Article

Synthesis and Characterization of Bioactive Magnetic Nanoparticles from the Perspective of Hyperthermia Applications

Elena-Alina Moacă [1,2], Vlad Socoliuc [3,4,*], Dana Stoian [5,*], Claudia Watz [1,2], Daniela Flondor [1,2], Cornelia Păcurariu [6], Robert Ianoș [6], Cristiana Iulia Rus [6], Lucian Barbu-Tudoran [7,8], Alexandra Semenescu [1,2], Cristian Sarău [5], Adelina Chevereșan [5] and Cristina Adriana Dehelean [1,2]

1   Faculty of Pharmacy, "Victor Babes", University of Medicine and Pharmacy Timisoara, 2nd Eftimie Murgu Square, RO-300041 Timisoara, Romania
2   Research Centre for Pharmaco-Toxicological Evaluation, "Victor Babes", University of Medicine and Pharmacy, 2nd Eftimie Murgu Square, RO-300041 Timisoara, Romania
3   Romanian Academy—Timisoara Branch, Center for Fundamental and Advanced Technical Research, Laboratory of Magnetic Fluids, 24 M. Viteazu Ave., RO-300223 Timisoara, Romania
4   Research Center for Complex Fluids Systems Engineering, Politehnica University of Timisoara, 1 M. Viteazu Ave., RO-300222 Timisoara, Romania
5   Faculty of Medicine, "Victor Babeş", University of Medicine and Pharmacy Timisoara, 2nd Eftimie Murgu Square, RO-300041 Timisoara, Romania
6   Faculty of Industrial Chemistry and Environmental Engineering, Politehnica University Timisoara, 2 Victoriei Square, RO-300006 Timisoara, Romania
7   Electron Microscopy Laboratory "Prof. C. Craciun", Faculty of Biology & Geology, "Babes-Bolyai" University, 5-7 Clinicilor Street, RO-400006 Cluj-Napoca, Romania
8   Electron Microscopy Integrated Laboratory, National Institute for R & D of Isotopic and Molecular Technologies, 67-103 Donat Street, RO-400293 Cluj-Napoca, Romania
*   Correspondence: vlad.socoliuc@upt.ro (V.S.); stoian.dana@umft.ro (D.S.)

Abstract: Magnetic iron oxide nanoparticles were obtained for the first time via the green chemistry approach, starting from two aqueous extracts of wormwood (*Artemisia absinthium* L.), both leaf and stems. In order to obtain magnetic nanoparticles suitable for medical purposes, more precisely with hyperthermia inducing features, a synthesis reaction was conducted, both at room temperature (25 °C) and at 80 °C, and with two formulations of the precipitation agent. Both the quality and stability of the synthesized magnetic iron oxide nanoparticles were physiochemically characterized: phase composition (X-ray powder diffraction (XRD)), thermal behavior (thermogravimetry (TG) and differential scanning calorimetry (DSC)), electron microscopy (scanning (SEM) and transmission (TEM)), and magnetic properties (DC and HF-AC). The magnetic investigation of the as-obtained magnetic iron oxide nanoparticles revealed that the synthesis at 80 °C using a mixture of NaOH and NH_3(aq) increases their diameter and implicitly enhances their specific absorption rate (SAR), a mandatory parameter for practical applications in hyperthermia.

Keywords: specific absorption rate; magnetic nanoparticles; green synthesis

1. Introduction

Cancer still remains a huge health concern worldwide, with an incidence, at the present time, of over 4.9 million of cases in Europe, from which there are over a hundred thousand cases in Romania. The incidences of cancer in Romania are expected to rise by 5.4% by 2030. According to global cancer observatory data, until now, deaths from cancer in Europe are over 2.2 million, fifty thousand of which are in Romania, and this is expected to rise by 7.6% by 2030 [1]. For this reason, in the last decade, significant measures have been developed for the diagnosis, monitoring, and therapy of cancer [2–6]. The diagnostic stage is primordial because the discovery of cancer in an early phase is determined by the choice of the most suitable and effective cancer therapy. Although it presents many disadvantages

and side effects [7–9], the viable conventional therapies used for cancer treatment are radiation therapy, chemotherapy, and surgery [10]. In consideration of the limited efficacy of viable conventional therapies, the development of new additional treatment approaches is strongly required. One antitumor therapy, which has been known and used for more than 30 years, is magnetic hyperthermia [11].

Hyperthermia is a therapeutic approach for cancer treatment and offers potential benefits for the treatment of many types of cancer, especially when used in combination with other therapies, such as chemotherapy [12,13], radiotherapy [14,15], or both [16,17]. Hyperthermia is based on an increase in temperature from 37 °C up to 45–46 °C, leading to the destruction of cancer cells by apoptosis, thus shrinking the tumors [18–20]. The great disadvantage of this therapeutic approach is the inability to heat only the tumor region, thus, by rising the temperature, normal cells are also affected [21]. Moreover, in solid tumors, internal heat dissipation takes place in the entire tumor mass, but this cannot adapt to such heat (45 °C), and the deep-seated tumor region overheats up to 50 °C [22]. However, by using various heat sources for hyperthermia purposes, specific body zones can be heated. By increasing temperature in a specific body zone, the therapeutic effect is maximized around the neighborhood of the respective body zone, while the undesirable side effects are minimized in the rest of the body zones [23]. The most investigated heating sources are magnetic nanoparticles, known as magnetic hyperthermia, which transform the electromagnetic energy given by an external high-frequency alternating (AC) magnetic field into heat [15]. Magnetic hyperthermia is a non-invasive treatment approach to cancer therapy that provides an alternative for certain types of cancers, especially for solid tumors [24], due to the fact that the AC magnetic field acts in the depth of the targeted tissues. In addition, this therapeutic technique allows the administration of concentrated magnetic nanoparticles that can stay, in certain conditions, around the tumor proximity, or in it, for repeated therapy sessions [25,26].

Among magnetic nanoparticles, magnetite (Fe_3O_4) and maghemite (γ-Fe_2O_3) are the most utilized nanomaterials for magnetic hyperthermia [27]. Due to their unique and distinctive physicochemical and biological features (superparamagnetic behavior, dimensions below 100 nm, large surface area-to-volume ratio, low toxicity, biocompatible with the human organism, easily controlled and modified surface functionalization, high heating efficiency), magnetite and maghemite are the most promising candidates used in magnetic hyperthermia therapy for cancer management [28–35]. Throughout time, various techniques have been applied to synthesize Fe_3O_4 and γ-Fe_2O_3, such as co-precipitation, thermal decomposition, laser pyrolysis, laser ablation, hydrothermal and solvothermal method, microemulsion, microwave radiation sol-gel, combustion, and the green method. Of all these techniques, the green method represent the simplest, most cost effective, and environmentally/biologically friendly alternative, and it has gained ground lately for the fabrication of magnetic nanoparticles compared with chemical or physical methods [36]. The green chemistry method allows the utilization of different bio-entities, such as plant extract, bacteria, viruses, algae, fungi, yeast, etc. [37–41]. Among all these biologic materials, plant extracts have the ability to reduce the metal precursor and stabilize the nanoparticles in a single-step method [42], and they are a harmless, cheap (often freely available), and easy to handle raw material. In addition, the phytocompounds from plant extracts (carbohydrates, alkaloids, amino acids, flavonoids, proteins, saponins, tannins, terpenoids, aromatic/nitrogenous compounds) also work in the same way as redox mediators and capping agents for the nanoparticles [38,41,43]. Many studies have clarified that the features of synthesized magnetic nanoparticles from plant extracts (dimension, shape, yield, phase composition, stability) [44–47], mainly depend on various parameters (type of plant extract, metal salt concentration, volume ratio of the extract to metallic salt precursor, presence or absence of precipitation agent, and reaction conditions: pH, temperature and incubation time) [42,47–49]. For example, it is well known that varying the extract amount in the reaction medium significantly influences the shape of the synthesized nanoparticles, while by varying the extract concentration, one can influence the size of the synthesized

nanoparticles. By varying the pH of the reaction medium, one can change the size and shape of the synthesized nanoparticles; larger nanoparticles can be obtained at low pH. The reaction time has an influence on the size and yield of nanoparticles, while reaction temperature influences the shape, size, and yield of the synthesized nanoparticles from plant extracts [49–52]. Regarding the type of plant extract, the multitude of biologically active compounds and their subsequent interaction with metallic precursor are the main factors that contribute to the diversity of the obtained nanoparticle size and shape. Considerable efforts have been dedicated lately to the design of superparamagnetic nanoparticles from various plant extracts, with complex functional features, which provide a high potential use in the biomedical field [48].

Artemisia absinthium L. (Asteraceae), commonly known as wormwood (W), has a plethora of bioactive phytoconstituents, such as phenols, terpenoids, flavonoids, coumarins, acetylenes, and sterols [53,54]. These bioactive phytoconstituents extracted from wormwood possess several therapeutic effects: digestive, insects repellent, antiprotozoal, anthelmintic, antibacterial, antifungal, anti-inflammatory, cytotoxic, antioxidative, neuroprotective, and wound healing [55–60].

This study was started with the aim of investigating to what extent the magnetic nanoparticles obtained by the green chemistry approach possess magnetic hyperthermia features, so that they can be used for the development of new therapeutic strategies that contribute to the improvement of current cancer therapies. In order to be suitable for medical purposes, the synthesized magnetic nanoparticles must be sensitive to heat, possess strong magnetic properties to allow them to be directed through the blood system, and have suitable dimensions and high specific surface to allow the attachment of other antitumor compounds. Therefore, the purpose of the current study consists of:
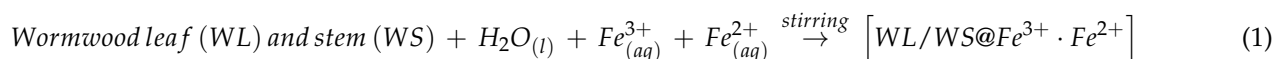
1. the fabrication of magnetic iron oxide nanoparticles through the green chemistry approach, starting from an aqueous extract of wormwood (*Artemisia absinthium* L.) based on leaves and stems, respectively;
2. the characterization of the preformed magnetic iron oxide nanoparticles through physicochemical analyzes;
3. the evaluation of hyperthermic efficacy of the preformed magnetic iron oxide nanoparticles by determining the specific absorption rate (SAR).

To date, several studies [61–68] have been reported in the literature in which magnetite and/or maghemite were synthesized by the green method, designed for hyperthermia applications, but none of them have evaluated the magnetic nanoparticles obtained as such from the synthesis. In addition, no study has been reported regarding the employment of wormwood for the fabrication of magnetic nanoparticles used for magnetic hyperthermia applications. Therefore, we can affirm that this is the first research study in which is detailed the biosynthesis of magnetic iron oxide nanoparticles using an aqueous extract of wormwood based on leaves and stems, designed for magnetic hyperthermia applications.

2. Results and Discussion

2.1. Samples Description

Two types of magnetic iron oxide nanoparticles were fabricated by the green chemistry approach at 25 °C and at 80 °C, coated with phytocompounds extracted from an aqueous extract of wormwood leaves (WL 25 and WL 80) and stems (WS 25 and WS 80), respectively. The parameters of the synthesis reaction were identical, with the exception of the precipitation agent—the first set of nanoparticles were obtained when a mixture of NaOH 1M and $NH_3(aq)$ 25% precipitation solutions was used, and for the second set of nanoparticles, only $NH_3(aq)$ 25% precipitation solution was used. The chemical reaction regarding the formation and precipitation of Fe_3O_4 is given in Equations (1) and 2.

$$Wormwood\ leaf\ (WL)\ and\ stem\ (WS)\ +\ H_2O_{(l)}\ +\ Fe^{3+}_{(aq)}\ +\ Fe^{2+}_{(aq)}\ \overset{stirring}{\rightarrow}\ \left[WL/WS@Fe^{3+}\cdot Fe^{2+}\right] \qquad (1)$$

$$\left[WL/WS@Fe^{3+}\cdot Fe^{2+}\right] + 8OH^-_{(aq)} \xrightarrow{\text{stirring}} \left[WL/WS@Fe_3O_4\right]_{(s)} + 4H_2O_{(aq)} \qquad (2)$$
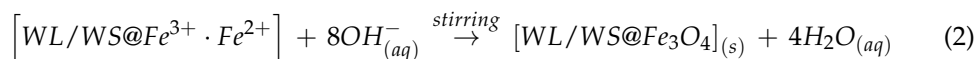
Table 1 describes the reagents used and the parameters of the synthesis reactions.

Table 1. Description of the synthesis conditions used for the preparation of iron oxide nanoparticles.

Nanoparticles Denomination	Reaction Synthesis Characteristics	Precipitation Agent	Observations
WL 25	Fe^{3+}:Fe^{2+} = 2.7	NaOH 1M + NH₃(aq) 25%	wormwood aqueous leaf extract
WS 25	10 mg/mL wormwood aqueous extract Volume ratio of metal precursor solution: plant extract = 1:1 Reaction medium temperature = 25 °C		wormwood aqueous stems extract
WL 80	Fe^{3+}:Fe^{2+} = 2.7 10 mg/mL wormwood aqueous extract Volume ratio of metal precursor solution: plant extract = 1:1		wormwood aqueous leaf extract
WS 80	Reaction medium temperature = 80 °C		wormwood aqueous stems extract
WL 25-2	Fe^{3+}:Fe^{2+} = 2.7	NH₃(aq) 25%	wormwood aqueous leaf extract
WS 25-2	10 mg/mL wormwood aqueous extract Volume ratio of metal precursor solution: plant extract = 1:1 Reaction medium temperature = 25 °C		wormwood aqueous stems extract
WL 80-2	Fe^{3+}:Fe^{2+} = 2.7 10 mg/mL wormwood aqueous extract Volume ratio of metal precursor solution: plant extract = 1:1		wormwood aqueous leaf extract
WS 80-2	Reaction medium temperature = 80 °C		wormwood aqueous stems extract

2.2. Physicochemical Properties of Magnetic Iron Oxide Nanoparticles Obtained via the Green Chemistry Approach

2.2.1. Phase Composition and Structural Characterization

Figure 1 exhibist the XRD spectra of the magnetic nanoparticles synthesized with two wormwood aqueous extracts from leaves (WL) and stems (WS), at two synthesis temperatures (25 °C and 80 °C) and a mixture of NaOH 1M and NH₃(aq) 25% as a precipitating agent. The XRD patterns of the resultant magnetic nanoparticles were found to resemble the characteristic magnetite nanoparticles pattern (PDF: 190,629). The diffraction peaks resulted from the XRD analysis are located at 2θ values around 18.12°, 30.18°, 35.49°, 43.31°, 53.57°, 57.14°, 62.78°, 71.25°, and 74.22°, in agreement with the reference peaks of magnetite, corresponding to (111), (220), (311), (400), (422), (511), (440), (533), and (444) Bragg's planar reflections, respectively. The crystallite size of the prepared samples seems to be influenced by the temperature and extract type. In the case of the samples fabricated from the aqueous extract of wormwood leaves, the crystallite size increases from 3 nm (WL 25) to 7 nm (WL 80) as the synthesis temperature increased from 25 °C to 80 °C. In the case of wormwood stem-derived samples, the crystallite size changed from 7 nm (WS 25) to 9 nm (WS 80), as the synthesis temperature increased from 25 °C to 80 °C.

Figure 2 exhibits the XRD spectra of the samples prepared using the same wormwood aqueous extracts from leaves and stems, at the same synthesis temperatures (25 °C and 80 °C), but with only NH₃(aq) as the precipitating agent. As in the previous case presented, the XRD patterns of the resultant magnetic nanoparticles were also found to resemble the characteristic magnetite nanoparticle pattern. The diffraction peaks resulted are located at 2θ values around 18.31°, 30.18°, 35.49°, 43.11°, 53.5°, 57.14°, 62.88°, 71.52°, and 74.46°, corresponding to (111), (220), (311), (400), (422), (511), (440), (533), and (444) Bragg's planar reflections, respectively. One can observe that, unlike when using NaOH and NH₃(aq) mixtures as precipitating agents, the samples precipitated with NH₃(aq) only exhibit lower crystallite size. The diameter of the magnetic nanoparticle crystallites at room temperature ranged from 1 to 7 nm. When NH₃(aq) was used as the precipitation agent, the crystallinity of the magnetic nanoparticles, given by the sharp peaks shown in Figure 2, are marked only for the nanoparticles fabricated from the aqueous extract of wormwood stems at

25 °C and 80 °C (WS 25-2 and WS 80-2) and for the nanoparticles WL 80-2, fabricated from aqueous extract of wormwood leaf at 80 °C. The XRD pattern of the sample fabricated at 25 °C from the aqueous extract of wormwood leaf (WL 25-2), using NH_3(aq) as the precipitation agent, suggest that the sample is practically amorphous, due to the lack of marked diffraction peaks.

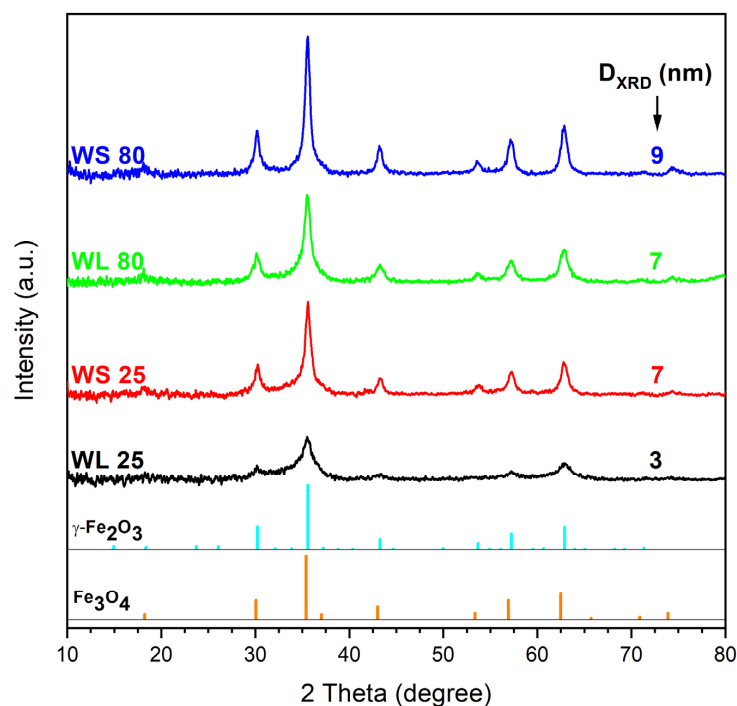**Figure 1.** XRD pattern of the iron oxide nanoparticles obtained from wormwood leaves (WL) and stems (WS) aqueous extracts, at 25 °C and 80 °C, using NaOH and NH_3(aq) as precipitation agents.
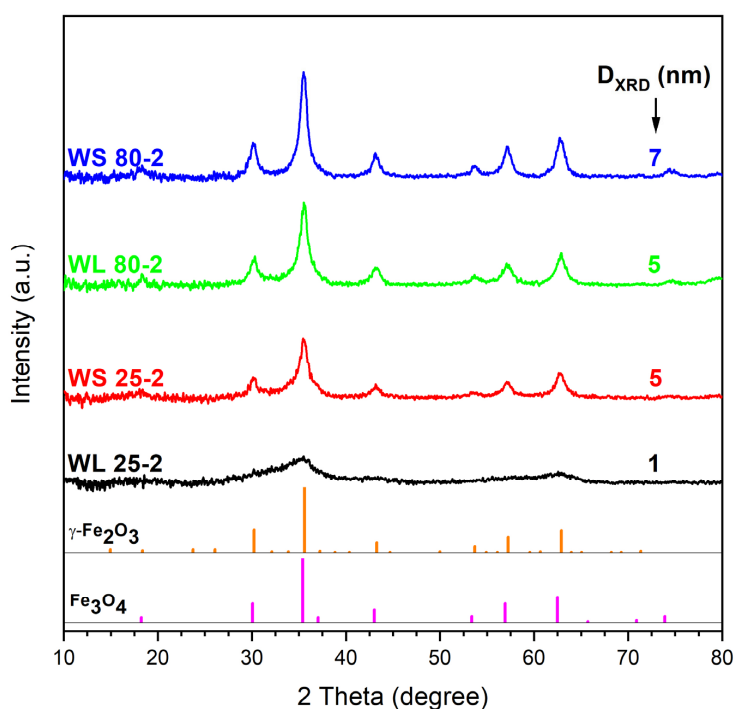

Figure 2. XRD pattern of the iron oxide nanoparticles obtained from the aqueous extracts of wormwood leaves (WL) and stems (WS), at 25 °C and 80 °C, using NH_3(aq) as the precipitation agent.

In terms of phase composition, the XRD patterns have not revealed significant differences among the prepared samples. With one exception (WL 25-2), all samples showed the inverse spinel structure of cubic magnetite or maghemite, regardless of the precipitating agent used [69]. These results are in agreement with those of other researchers [70–74].

Karthik et al. [75] demonstrated that the amorphous nature of the nanoparticles is not toxic for living organisms. Moreover, they showed that the amorphous nanoparticles obtained from plant extracts have an enhanced biocompatibility for different applications, which is a mandatory requirement for the biomedical field. Regarding the purity of the synthesized samples, one cannot neglect the fact that the diffraction peaks of Fe_3O_4 and γ-Fe_2O_3 are very close. Therefore, one cannot exclude the presence of both compounds. According to Kim et al. [76], it is very possible that, during the synthesis (for 2 h), the partial oxidation of magnetite to maghemite occurs. Consequently, it is most likely that each sample contains a mixture of magnetite (predominant phase due to the strong magnetic moment and black color of the samples) and maghemite (probably in traces).

2.2.2. Thermal Behavior

Figure 3 shows the TG−DSC graphs of magnetic nanoparticles synthesized using the leaves and stems of wormwood aqueous extracts and a mixture of NaOH and NH_3(aq) as precipitation agents. Regardless of the aqueous extract or the temperature of obtaining the magnetic nanoparticles, the TG−DSC curves indicate there are no major differences between the samples. At low temperature (below 100 °C), water evaporation takes place, as evidenced by the endothermic effect accompanied by a mass loss on the TG curve. The total weight loss percentage was higher when the magnetic nanoparticles were obtained at 25 °C compared to those obtained at 80 °C (WL: 20.44% vs. 14.34%; WS: 13.78% vs. 10.92%). Between 200 °C and 300 °C, all four DSC curves show two overlapped exothermic effects. These effects are accompanied by a significant mass loss on the TG curve and most likely are related to the oxidation of the organic compounds contained in the vegetal product (wormwood leaf and stem aqueous extracts). In the same temperature range, magnetite is most-likely oxidized to maghemite. In the case of sample WL 25, one can observe small exothermic effect at 514.0 °C, accompanied by a low mass loss of 1.05%. This effect could be related to maghemite–hematite polymorph transition.
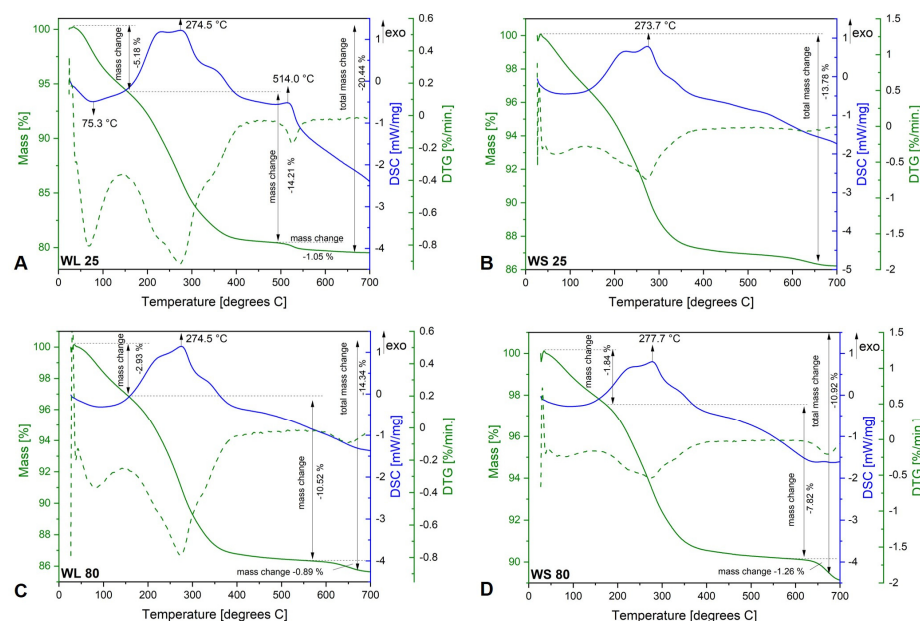

Figure 3. TG−DSC/DTG curves of iron oxide nanoparticles obtained from aqueous extracts of wormwood leaves (WL) and stems (WS), at 25 °C (**A**,**B**) and 80 °C (**C**,**D**), via the green chemistry approach, using NaOH and NH_3(aq) as the precipitation agents.

The TG−DSC curves of the samples synthesized using the aqueous extracts of the leaves and stems of wormwood and only NH_3(aq) aqueous solution as the precipitation agent are depicted in Figure 4. As in the case of the previous set of samples, the mass loss taking place below 100 °C is related to water removal. The largest weight loss occurs in the range 100–500 °C and can be ascribed to the decomposition of the organic biomolecules contained in the plant extract and capped on the magnetic nanoparticles' surface. Both overlapped exothermic effect are also recorded in this case, between 200–300 °C, probably due to the oxidation/degradation of the organic phytocompounds from plant extracts (aqueous extracts of wormwood leaves and stems). In the case of the WL 25-2 sample, one can observe an exothermic effect at 507.7 °C, accompanied by a weight loss of 13.68%. This phenomenon could be attributed to the maghemite–hematite transformation as well as to the conversion of one or more aromatic amino-acids and/or carbohydrates from the wormwood leaf aqueous extract into various secondary metabolites. In the case of the WS 80-2 sample, the small exothermic effect at 666.7 °C, accompanied by a low mass loss of 0.92%, is assigned to the oxidation of the carbon content present in the sample, from the organic phytocompounds.
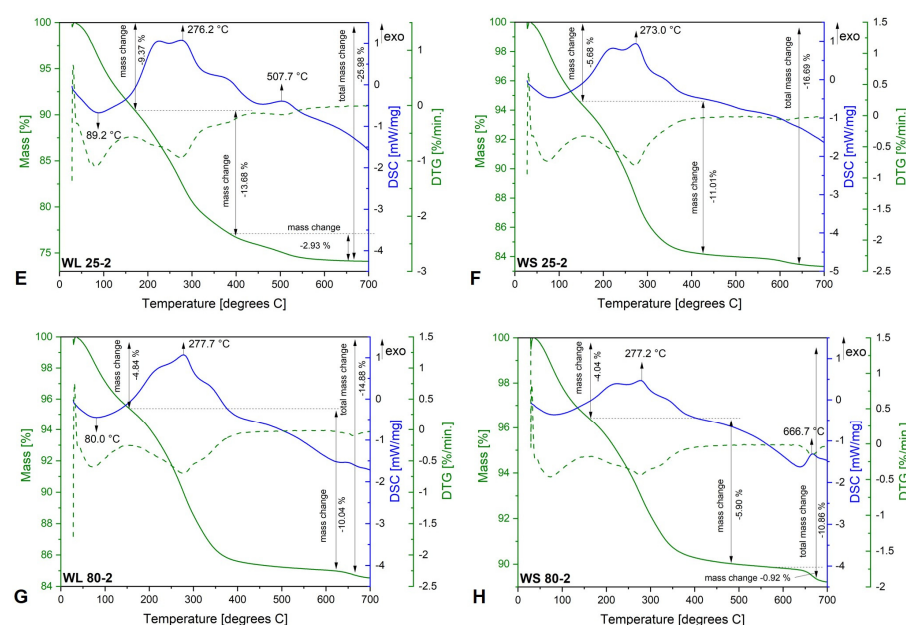

Figure 4. TG−DSC/DTG curves of iron oxide nanoparticles obtained from the aqueous extracts of wormwood leaves (WL) and stems (WS), at 25 °C (**E,F**) and 80 °C (**G,H**), via the green chemistry approach, using NH_3(aq) as the precipitation agent.

The thermal behavior of the magnetic nanoparticles gives additional information regarding the mass change with temperature and their stability as a function of temperature. Regarding the thermogravimetric curves of all magnetic nanoparticles prepared, the mass loss consists of three stages, from which the first weight loss up to 150 °C is attributed to nanoparticle water surface loss and/or other unstable bioactive compounds [77]. In all cases, it can be observed that the total mass loss decreases with the increase in synthesis temperature. The highest weight loss up to 500 °C takes place in the second stage, accompanied by various exothermic effects, attributed to the decomposition/degradation of aromatic amino-acids and/or carbohydrates from the wormwood leaf aqueous extract, into various secondary metabolites. The physicochemical profile of a Romanian wormwood extract was established and reported by our research group [56]. Therefore, the exothermic effect observed after 600 °C (WS 80-2) (Figure 4H), attributed to the carbon oxidation from organic biomolecules and the total weight loss recorded in all the samples, confirms the fact that the formed iron oxide magnetic nanoparticles have biologically active compounds from the plant extract, either on their surface or in their pores [78].

2.2.3. Electron Microscopy Characterization

In Figures 5 and 6 are depicted the SEM representative images of the magnetic nanoparticles obtained via the green chemistry approach, starting from both the aqueous extracts of wormwood leaves (WL) and stems (WS), at 25 °C and 80 °C, and using either a mixture of NaOH and NH_3(aq) (Figure 5) or only NH_3(aq) (Figure 6), respectively. The morphology of the synthesized magnetic nanoparticles was almost similar in all cases, regardless of the reaction medium temperature and/or precipitation agent used. At first glance, one can observe that the magnetic sample obtained when the precipitation agent used was NH_3(aq) appears more porous (Figure 6). This aspect could be due to the amount of capping compounds from the plant extract.

Figure 5. SEM images of magnetic iron oxide nanoparticles obtained from the aqueous extracts of wormwood leaves (WL) and stems (WS), at 25 °C (**A**,**B**) and 80 °C (**C**,**D**), via the green chemistry approach, using NaOH and NH_3(aq) as the precipitation agents.
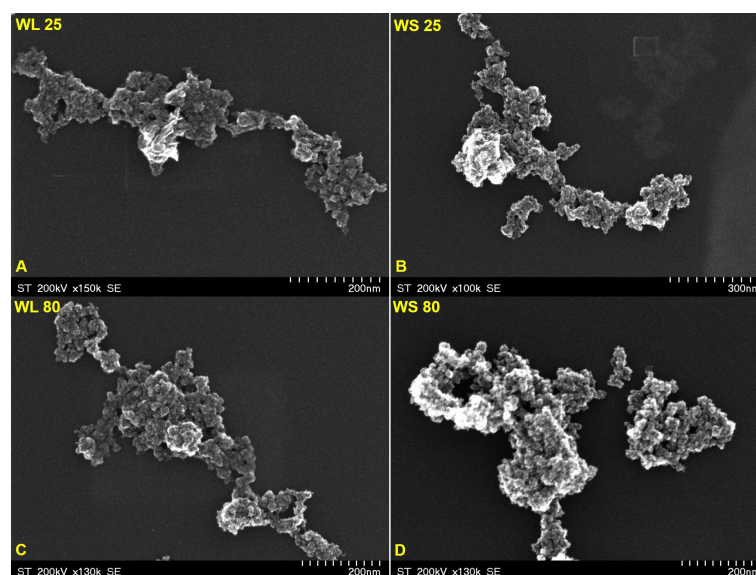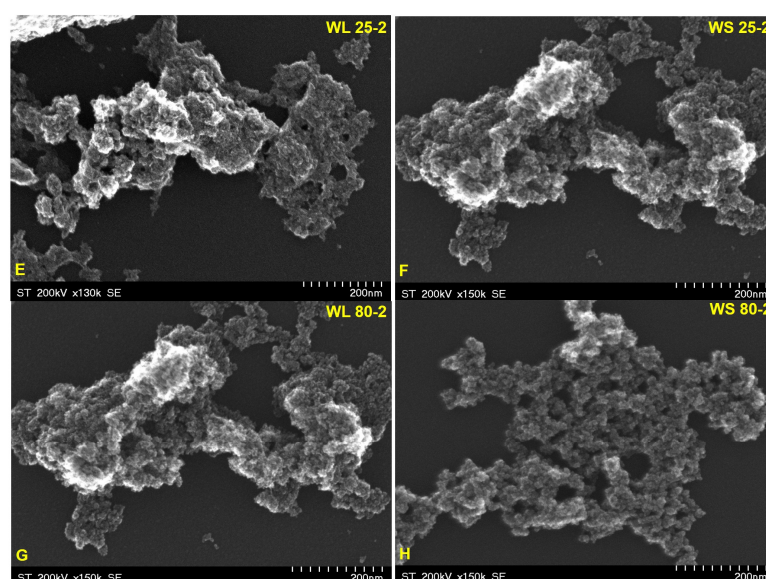

Figure 6. SEM images of magnetic iron oxide nanoparticles obtained from the aqueous extracts of wormwood leaves (WL) and stems (WS), at 25 °C (**E**,**F**) and 80 °C (**G**,**H**), via the green chemistry approach, using NH_3(aq) as the precipitating agent.

In addition, the SEM images show nanoparticles of phase uniformity with a very similar spherical shape and particle size in the range of 1–10 nm. A slight agglomeration can be observed in all cases, but this could be due to the large surface area to volume ratio and bridge interactions among organic molecules adsorbed on the nanoparticles.

Figures 7 and 8 provide information regarding the chemical composition of each prepared sample by the green chemistry approach. EDX analysis revealed iron and oxygen as major components, which confirmed the formation of Fe_3O_4 nanoparticles. The excess presence of carbon in all samples is due to the tape used as the grid support for the immobilization of the magnetic particles as well as to the residual organic compounds from plant extracts. Besides carbon, one can observe other chemical elements (chlorine—Cl, calcium—Ca, and silicon—Si) present in a neglected total weight percent, which most likely come from the growing soil of the plant. Cl appears only for the samples prepared at 25 °C, regardless of the precipitation agent used or the plant's organ from which the extract was obtained. One can say that this element could also come from unreacted metal salt ($FeCl_3$). Nonetheless, these elements can be neglected because their total weight percentages are in very small quantities.
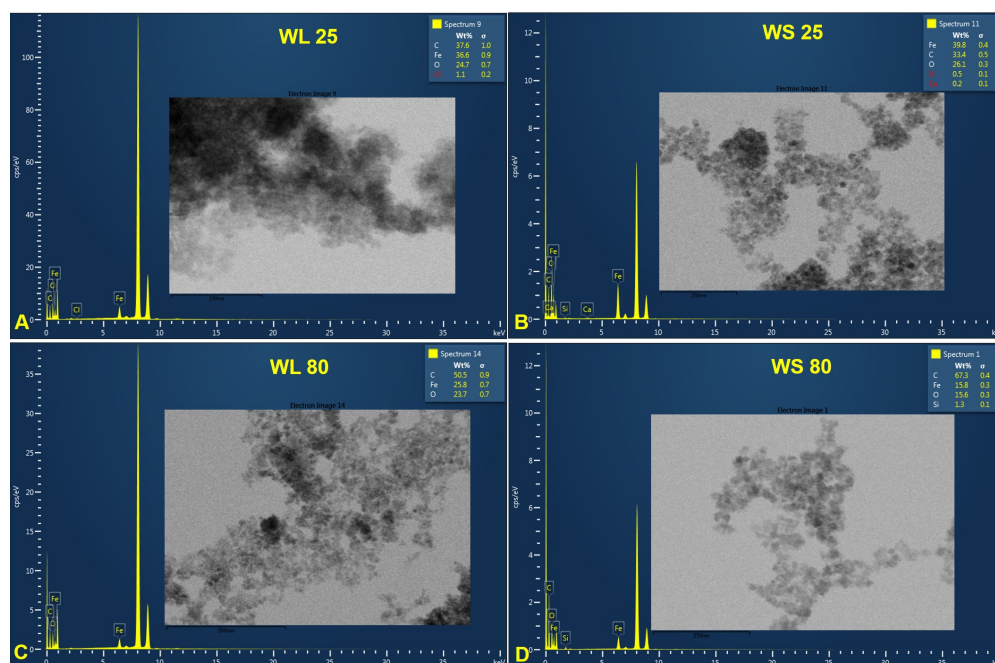

Figure 7. EDX spectra of magnetic iron oxide nanoparticles obtained from the aqueous extracts of wormwood leaves (WL) and stems (WS), at 25 °C (**A**,**B**) and 80 °C (**C**,**D**), via the green chemistry approach, using NaOH and NH_3(aq) as the precipitation agents.

One aspect worth highlighting is the total weight percentage (wt%) of Fe. One can observe that, regarding the magnetic nanoparticles formed from the aqueous extracts of wormwood leaves and stems precipitated with a mixture of NaOH and NH_3(aq) aqueous solutions, the wt% of Fe decreases with the increase in temperature, from 25 °C (36.6%) to 80 °C (25.8%) (Figure 7). The same phenomenon occurred when the wormwood aqueous extract based on stems was precipitated only with NH_3(aq) (Figure 8F,H). Instead, in the case of the wormwood aqueous extract based on leaf, precipitated only with NH_3(aq), increasing the temperature in the reaction medium had no effect on the change in the total weight percentage of iron (Figure 8E,G). The EDX spectra recorded the presence of iron peaks in three different areas, at approximately 0.8, 6.2, and 7.0 keV.
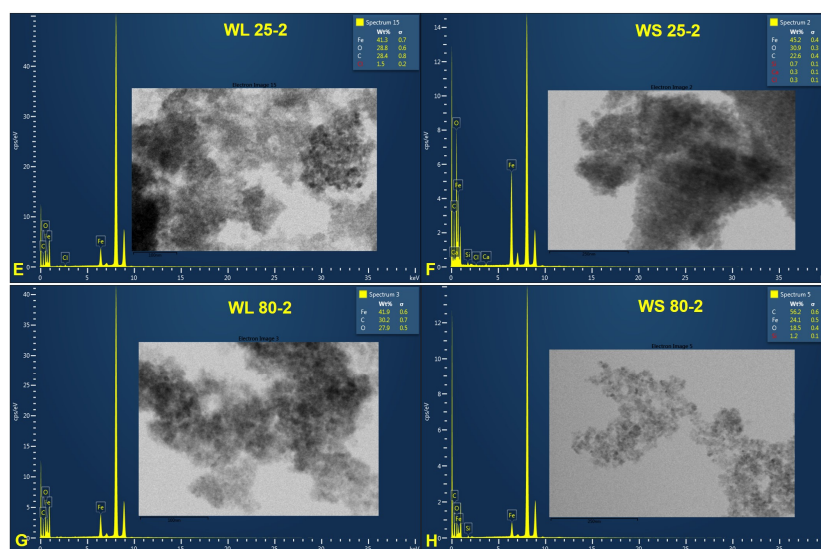
Figure 8. EDX spectra of magnetic iron oxide nanoparticles obtained from the aqueous extracts of wormwood leaves (WL) and stems (WS), at 25 °C (**E**,**F**) and 80 °C (**G**,**H**), via the green chemistry approach, using NH_3(aq) as the precipitation agent.

Figures 9 and 10 depict the TEM images of the synthesized magnetic nanoparticles by the green chemistry approach, starting from two wormwood aqueous extracts based on leaves and stems. The results confirm the almost spherical shape and the formation of Fe_3O_4 at nanometric scale (particles size under 10 nm), by a simple and economic approach. Regarding the nanoparticles formed by using NH_3(aq) as the precipitation agent (Figure 10), one can observe that the nanoparticles were more agglomerated (especially when the synthesis occurs at 25 °C), which is probably due to the phytocompounds presents in the wormwood aqueous extract, especially the hydroxyl groups (polyphenols). The particle sizes determined by TEM analysis are in agreement with the calculated crystallites sizes (Figures 1 and 2) from the Debye–Sherrer Equation (3), meaning that all the samples are composed of uniformly single crystals.

Figure 9. TEM images of magnetic iron oxide nanoparticles obtained from the aqueous extracts of wormwood leaves (WL) and stems (WS), at 25 °C (**A**,**B**) and 80 °C (**C**,**D**), via the green chemistry approach, using NaOH and NH_3(aq) as the precipitation agents.
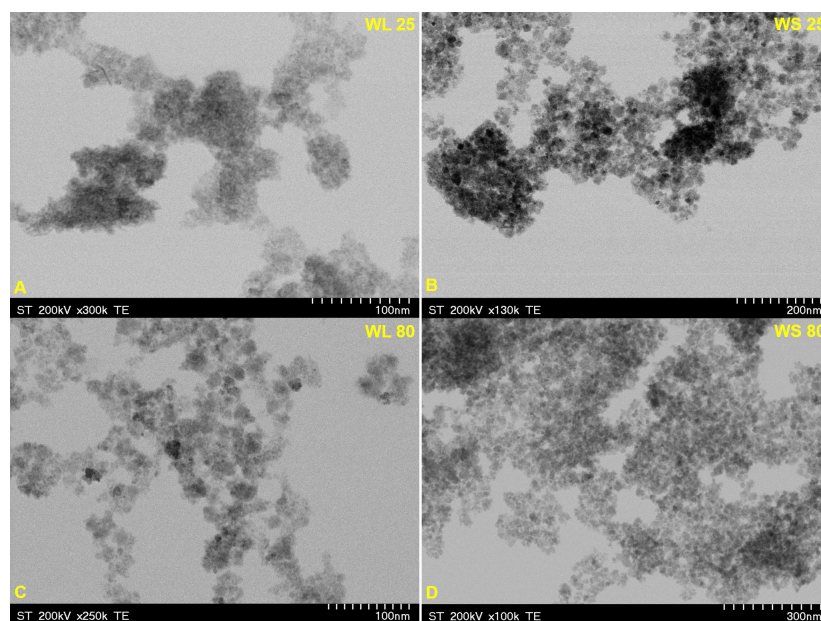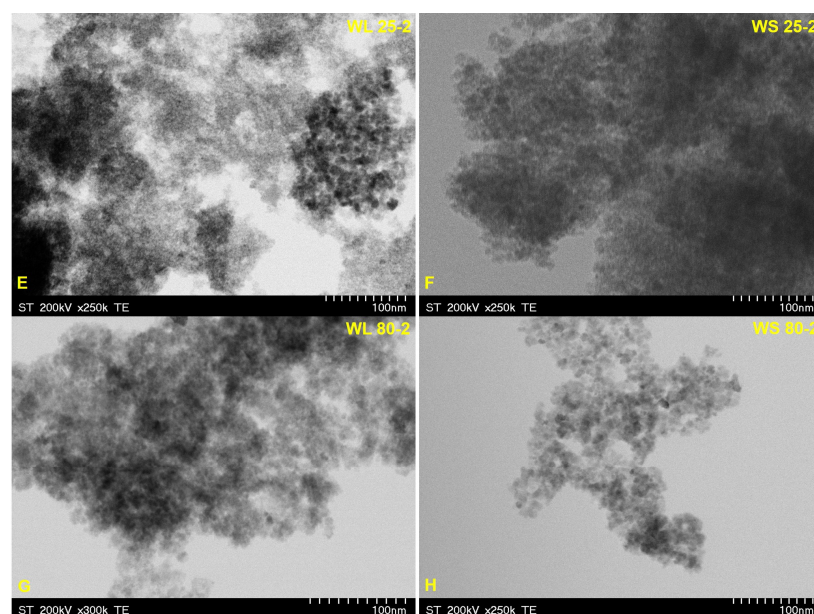
Figure 10. TEM images of magnetic iron oxide nanoparticles obtained from the aqueous extracts of wormwood leaves (WL) and stems (WS), at 25 °C (**E,F**) and 80 °C (**G,H**), via the green chemistry approach, using NH_3(aq) as the precipitation agent.

Morphological characterization and sizing of the synthesized magnetic nanoparticles were carried out through SEM and TEM analysis. The SEM and TEM images (Figures 5, 6, 9 and 10) revealed that the magnetic nanoparticles prepared are of phase uniformity, with an almost spherical shape and particle size under 10 nm. Our results are similar to those reported in the literature [70,71,79–81]. Due to nanoparticle stacking on the grid, the TEM images are too blurred to be used for granulometry. Therefore, the SEM images were used for granulometry. Using ImageJ (https://imagej.nih.gov/ij/index.html, accessed on 19 October 2022), more than 200 nanoparticles were measured from each sample. Nanoparticle mean diameter and standard deviation are presented in Table 2. Generally, the polyphenols contained in the plant extract are responsible for the formation of the crystalline phase, very similar to the Fe_3O_4 structure. The high concentration of polyphenols in the plant extract is also responsible for obtaining nanoparticles with a narrow size [62]. However, it is very likely that, at the same time, an increased amount of the plant extract used can lead to the abundant presence of bioactive compounds (polyphenols), which leads to oxidation of the surface of the formed nanoparticles (due to additional water molecules), in addition to covering them, thus forming Fe_3O_4—γ-Fe_2O_3 [62].

Table 2. Magnetic characteristics of the samples.

No.	Sample Denomination	M_{sat}@1MA/m (Am^2/kg)	M_r/M_{sat} (-)	H_c (kA/m)	D_m (nm)	D_{SEM} (nm)	D_{XRD} (nm)	SAR_{max} (W/kg)
1	WL 25	20.4	0.98×10^{-3}	0.013	$1.2 \pm. 1.0$	4.3 ± 0.8	3	439
2	WS 25	41.9	1.12×10^{-3}	0.038	5.8 ± 2.2	6.5 ± 2.1	7	880
3	WL 80	45.9	0.22×10^{-3}	0.015	5.3 ± 2.2	7.6 ± 2.9	7	650
4	WS 80	61.4	3.58×10^{-3}	0.125	6.9 ± 1.8	9.1 ± 2.9	9	904
5	WL 25-2	9.9	0	0	0.3 ± 0.2	3.5 ± 0.8	1	0
6	WS 25-2	36.7	19.1×10^{-3}	0.800	3.2 ± 2.0	6.1 ± 1.8	5	253
7	WL 80-2	53.4	1.31×10^{-3}	0.100	4.2 ± 2.0	4.8 ± 1.3	5	473
8	WS 80-2	61.9	0.48×10^{-3}	0.018	5.2 ± 1.9	7.5 ± 2.5	7	520

By corroborating the morphological aspects (Figure 10) with the nanoparticles' narrow size given by SEM, it is possible that the use of the NH_3(aq) aqueous solution does not

precipitate enough nanoparticles, and hence very small nanoparticles are obtained. Another explanation could be related to the growth time of nuclei as well as the variation in the composition and concentration of the bioactive molecules contained in different plants' organs and the subsequent interaction of these biomolecules with metal ions from the aqueous solution. It is believed that the latter is the main parameter that strongly influences the obtaining of nanoparticles with different sizes and shapes [82]. It was showed that a higher amount of bioactive compounds in a plant extract led to the decrease in particle size [83]. In addition, the formation of nanoparticles is proportional to their dimensions, i.e., the faster the nanoparticle formation is, the smaller the nanoparticles obtained [84].

The agglomeration of the nanoparticles depends on many factors being a determined parameter for size and shape of the resulted nanoparticles. According to Cruz et al., regarding the synthesis of nanoparticles from a plant extract, the increasing of reaction temperature is accompanied by an increase in the efficiency of the metal ion reduction [85]. In addition, it was suggested that the H-bonding present in various bioactive reducing agents from leaf plant extracts could be the reason for the nanoparticle agglomeration [86]. This aspect is in agreement with our results from EDX, in which it was showed that the iron total weight percent decreases with the temperature increase (Figures 7 and 8) as well as with SEM/TEM images (Figures 5, 6, 9 and 10).

2.2.4. Magnetic Investigations

The iron oxide nanoparticles' magnetic properties were investigated in the DC magnetic field by means of vibrating sample magnetometry (VSM) and in the high-frequency AC magnetic field by means of induction heating experiments.

The DC hysteresis and initial magnetization curves of the iron oxide nanoparticles were measured by means of VSM at room temperature in the 0–1000 kA/m magnetic field intensity range. The initial magnetization curves of the iron oxide nanoparticles are shown in Figure 11A, together with the theoretical fits with a theoretical model for the dense dispersions of superparamagnetic nanoparticles (see Section 3.3). The fit R^2 was better than 0.999 for all samples, which proves the superparamagnetic nature of the as-obtained magnetic nanoparticles. Table 2 summarizes the nanoparticles' magnetic properties: saturation magnetization (M_{sat}), remanent magnetization (M_r), coercive field (H_c), and magnetic diameter (D_m).

Figure 11. (**A**) First magnetization curves of the samples; (**B**) Samples' SAR dependence on the AC magnetic field amplitude H_0.

The AC magnetic field amplitude (H_0) dependence of the samples' magnetic specific absorption rate (SAR) is presented in Figure 11B. The samples' maximum SAR at $H_0 = 1$ kA/m is tabulated in Table 2.

For further analysis purposes, Table 3 shows the Pearson correlation coefficient matrix of SAR, M_{sat}, D_m, D_{SEM}, and D_{XRD}.

Table 3. Pearson correlation coefficient matrix of SAR, M_{sat}, D_m, D_{SEM}, and D_{XRD}.

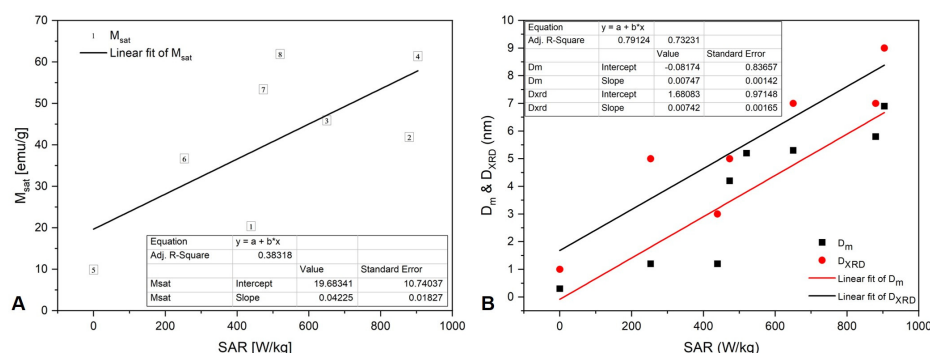|	**SAR**	**M_{sat}**	**D_m**	**D_{SEM}**	**D_{XRD}**
SAR	1	0.687	0.878	0.761	0.878
M_{sat}	0.687	1	0.902	0.808	0.892
D_m	0.878	0.902	1	0.902	0.983
D_{SEM}	0.761	0.808	0.902	1	0.952
D_{XRD}	0.878	0.892	0.983	0.952	1

The magnetic diameter of the nanoparticles, D_m, is the main characteristic that determines their magnetic properties, both DC and AC. The magnetic diameter is smaller than the physical diameter, D_{SEM}, due to the dead magnetic layer at the surface of the magnetic nanoparticles. The dead magnetic layer is caused by the loss of spin correlations at the surface [87] and the oxidation and chemical interactions with surface adsorbed molecules [88]. As one can see from Table 3, the samples' magnetic diameter is fairly well correlated with the saturation magnetization and SEM-diameter, and is even better correlated with the XRD diameter. At both synthesis temperatures, nanoparticles synthesized in the presence of stem extract (WS) have a larger diameter and saturation magnetization than nanoparticles synthesized in the presence of leaf extract (WL) (Table 2).

The DC hysteresis curves reveal negligible remanence magnetization, M_r, and coercive field, H_c, in all samples. This is consistent with the low values of the nanoparticles' diameter found from SEM, XRD, and magnetogranulometry. The DC first magnetization curves reveal the iron oxide nanoparticles' clustering with respect to the saturation magnetization (Figure 11A). The synthesis at 80 °C leads to almost double saturation magnetization compared with the 25 °C temperature synthesis. Except for the WL 80 samples, the addition of NaOH mixed with NH_3(aq) as the precipitation agent increases the saturation magnetization, especially when the synthesis take place at 25 °C.

The AC magnetic heating experiments show that, except for WL 25-2 (the sample with the smallest diameter and saturation magnetization), which has zero SAR, all samples show a quasi-quadratic dependence on H_0. As with saturation magnetization, SAR is stronger in samples where NaOH mixed with NH_3(aq) was added as the precipitation agents and stem extract (WS) was used. However, unlike the saturation magnetization, SAR reveals a different clustering among the samples with respect to temperature: WS 25 is close to WS 80, and both have the greatest SAR efficiency. WS 25 has the largest magnetic diameter (5.8 nm) among the samples synthesized at 25 °C, comparable to that of the samples synthesized at 80 °C, but most likely the nanoparticles are covered with a nonmagnetic thick layer because its saturation magnetization is approximately half of WS 80. The nonmagnetic layer makes D_m rather than M_{sat} a better predictor for SAR, as can be seen in Table 3 and Figure 12. This is due to the fact that two samples with the same saturation magnetization can differ with respect to the weight of small and large particles. Due to the nonlinear dependence of SAR on nanoparticle volume, the sample with predominantly fewer but larger particles will have a greater SAR than the sample with predominantly more numerous but smaller particles.

Figure 12. SAR correlation with (**A**) M_{sat} and (**B**) D_m and D_{XRD}.

3. Materials and Methods

3.1. Materials

Iron (III) chloride hexahydrate ($FeCl_3 \cdot 6H_2O$) and iron (II) sulphate heptahydrate ($FeSO_4 \cdot 7H_2O$) were purchased from Merck, Darmstadt, Germany, as an analytical grade reagent and used without any further purification. Sodium hydroxide (NaOH) pellets and ammonium hydroxide (NH_3(aq) 25%) were acquired from Chemical Company SA, Iasi, Romania. All the solutions were prepared using ultrapure water from the Milli-Q® Integral Water Purification System (Merck Millipore, Darmstadt, Germany).

3.2. Preparation of Wormwood Aqueous Extract and Iron Oxide Nanoparticle Synthesis via the Green Chemistry Approach

The aqueous extract from the leaf and stems of wormwood (*Artemisia absinthium* L.) was obtained according to the protocol described in our previously reported study [89]. Regarding the iron oxide nanoparticle synthesis via the green chemistry approach, it followed the protocol described by Abdullah et al. [47], with some modifications. Briefly, 50 mL aqueous solution of iron (III) chloride hexahydrate and iron (II) sulphate heptahydrate in a molar ratio of 2.7 were mixed homogeneously in 50 mL of aqueous solution of wormwood extract (W), leaves (WL), and stems (WS), of 10 mg/mL, under magnetic stirring at various temperatures. Then, in some samples, a mixture of NaOH 1M and NH_3(aq) 25% (12.5 mL/each) was added drop wise to the metal precursor solution and plant extract. In the others, only NH_3(aq) 25% (25 mL) was added under continuous stirring, to ensure homogenous reaction. The whole mixture was stirred for 2 h at various temperatures. After cooling, the dark precipitate, obtained by magnetic separation, was washed three time with distilled water (200 mL/each wash) at room temperature; the nanoparticles were then dried in an air oven (POL-EKO Aparatura, Wodzisław Slaski, Poland) for several hours, at 70 °C. The samples are briefly detailed in Table 1 in the Results and Discussion section. Figure 13 exhibits the schematic representation, which demonstrates the possible interaction between Fe_3O_4 nanoparticles and bioactive compounds from leaf and stem aqueous wormwood extracts.
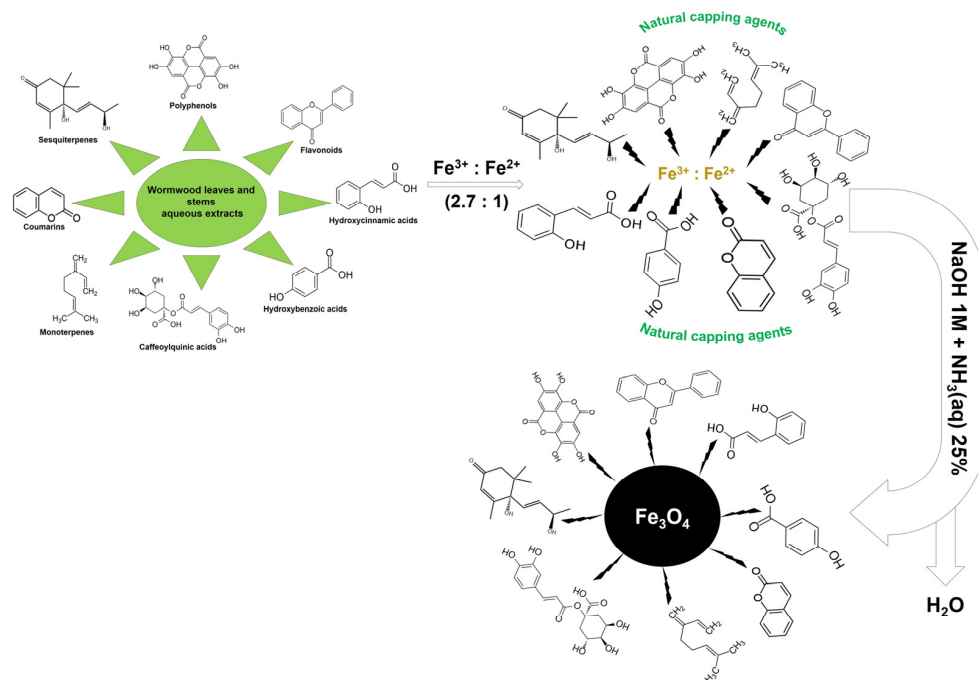

Figure 13. Possible mechanism of Fe_3O_4 nanoparticles synthesis via the green chemistry approach.

3.3. Physicochemical Characterization of Iron Oxide Nanoparticles

The synthesized iron oxide nanoparticles were characterized by different types of instruments. The phase composition of the nanoparticles was investigated using a Rigaku Ultima IV instrument (Rigaku Corporation, Tokyo, Japan), with CuKα radiation λ = 0.15406 nm at a voltage of 40 kV and a current of 40 mA. In order to investigate the crystalline nature of the nanoparticles, the scanning was performed at room temperature in the angular range of 10 to 80 °C, with a scan rate of 10°/minute. The crystallite size of the nanoparticles was calculated using the Debye–Scherer equation and the most intense peak (311):

$$D_{XRD} = \frac{0.9 \cdot \lambda}{\beta \cdot \cos\theta} \tag{3}$$

where D_{XRD} is the nanoparticles crystallite size (nm), λ is the radiation wavelength (nm), β is the full width at half of the maximum (radians), and θ is the Bragg angle (degree).

The following PDF files were used for the peak assignment: 391,346 (γ-Fe_2O_3) and 190,629 (Fe_3O_4), specific for maghemite and magnetite, from the International Centre for Diffraction Data Powder Diffraction File.

The stability of the nanoparticles was assessed by thermal analysis. The thermogravimetric (TG) and differential scanning calorimetry (DSC) data were obtained using the Netzsch STA 449 °C apparatus (Selb, Netzsch-Gerätebau GmbH, Germany), operating at temperatures ranging from 25 to 700 °C, at a heating rate of 10 °C/min., under an artificial air flow of 20 mL/min.

Cold field emission-scanning electron microscopy (SEM) was employed to observe the surface morphologies of the nanoparticles obtained. The nanoparticles, which were mounted on copper stubs as grid supports and sputter-coated with carbon, were examinated by SEM using the Hitachi SU8230 cold field emission gun STEM (Chiyoda, Tokyo, Japan) microscope, operating at an acceleration voltage of 30 kV in high-vacuum mode. The energy dispersive X-ray spectrometry (EDX) detector X-Max^N 80 (Oxford Instruments, Bristol, UK) was coupled to the microscope in order to perform the elemental analysis of the nanoparticles.

The size, shape, and morphology of nanoparticles were observed by transmission electron microscopy (TEM), using a Hitachi HD2700 cold field emission gun STEM (Chiyoda, Tokyo, Japan), equipped with two windowless EDX detectors (X-Max^N 100).

The magnetic properties of the nanoparticles were investigated by means of vibrating sample magnetometry (VSM) using a VSM 880 magnetometer (ADE Technologies, West-wood, MA, USA). Initial magnetization and hysteresis curves were measured at room temperature and external magnetic field in the range of 0–1000 kA/m. The initial magnetization curves were fitted with a theoretical model in order to determine the sample's magnetic nanoparticle statistics (i.e., magnetogranulometry). Details on the magnetogranulometry method can be found in [90]. The hysteresis curves were used to determine the magnetic nanoparticles' saturation magnetization (M_{sat}), remanent magnetization (M_r), and coercive field (H_c).

3.4. AC Magnetic Heating Efficiency of the Iron Oxide Nanoparticles

The heating efficiency of the magnetic nanoparticles was investigated via the specific absorption rate (SAR), using the standard procedure [91]. A commercially available induction heater was used (Figure 14), with magnetic field amplitude (H_0) in the range of 4–13 kA/m and 100 kHz frequency. A flat styrofoam sample holder contained in a 25 mm diameter PVC tube was axially mounted in the induction coil. The heat conduction coefficient of styrofoam (0.033 W/m/K) is very close to air (0.026 W/m/K at room temperature) [92]. The magnetic nanoparticles were pressed into cylindrical 5 mm diameter and ~1 mm height pellets. The pellets were placed in the middle of the induction coil, on the styrofoam sample holder. The magnetic field amplitude at the sample position was measured using a coil sensor. The pellet temperature (T) was measured with a Teledyne FLIR A40 thermal camera (Wilsonville, OR, USA) (Figure 14) during the heating process.
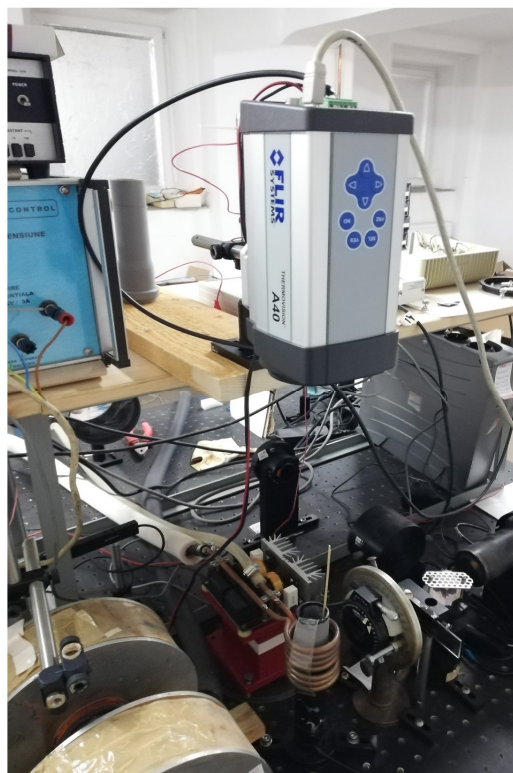
Figure 14. AC magnetic heating setup.

In Figure 15 are presented a print screen of the camera computer interface with the thermal image captured by the camera with sample and sample holder (ambient) measuring points (the top-left panel), as well as the time evolution of the measured temperatures (bottom panel: sample temperature in red and sample holder temperature in blue). The temperature increase rate (dT/dt) was determined by means of linear fitting of the T(t) data in the adiabatic regime, i.e., immediately after the AC field onset, before approximately 1 °C temperature increase (Figure 15, top-right panel).
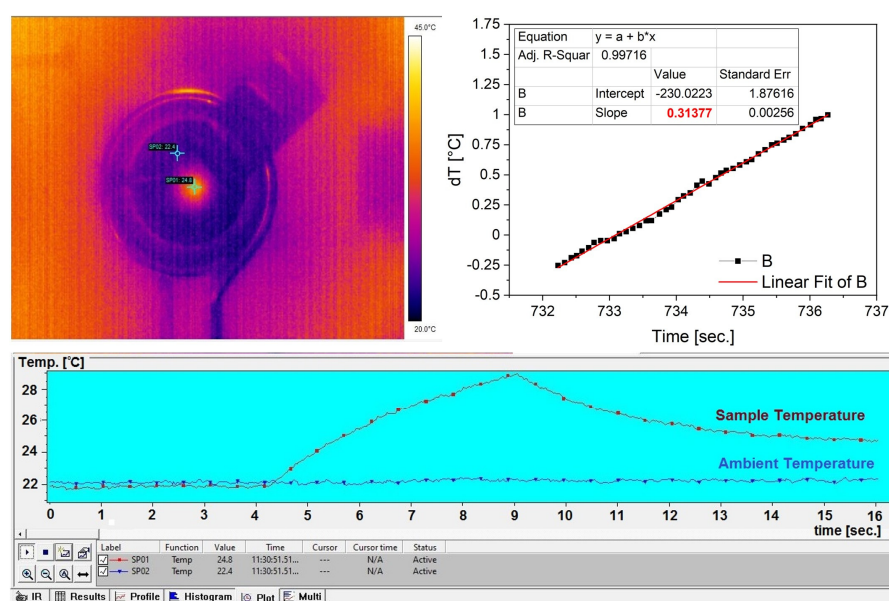

Figure 15. Camera computer interface thermal image (top−left panel) and temperature time evolution (bottom panel), and temperature increase rate determination (top−right panel).

4. Conclusions

In the present study, a simple and cost-effective green chemistry approach of magnetic nanoparticles with an average particle size under 10 nm is reported for the first time, starting from two aqueous extracts of wormwood, based on leaf and stem, respectively. In the plant-mediated green synthesis, the effect of precipitation agent was investigated, as was the reaction temperature, on both the fabrication of magnetic nanoparticles and on their heat generation under an external high-frequency alternating magnetic field. The nature of the precipitation agent used in the reaction synthesis and reaction temperature were varied, while the other participant components were kept constant, i.e., the amount and nature of the plant extract, the amount and molar ratio of Fe^{3+}:Fe^{2+}, and the volume ratio of metal precursor solution to plant extract. The magnetic investigations of the samples revealed that the synthesis at 80 °C using a mixture of NaOH and NH_3(aq) as precipitation agents leads to larger magnetic nanoparticles and implicitly more effective AC magnetic heating agents. Further research is needed in order to optimize the synthesis procedure, with the aim of increasing the nanoparticles' magnetic diameter and implicitly the AC magnetic heating efficiency, due to the fact that the practical applications of nanoparticles in hyperthermia are limited by their sizes. Nevertheless, we believe that this research opens new methods regarding the synthesis conditions taken into account for the preparation of biocompatible and highly stable magnetic nanoparticles via a plant-mediated green chemistry approach.

Author Contributions: Conceptualization, E.-A.M. and V.S.; methodology, E.-A.M., V.S., C.W., C.P., R.I., C.I.R., L.B.-T. and A.S.; software, E.-A.M., V.S., D.S., D.F., C.W., R.I., L.B.-T. and A.C.; validation, V.S., D.S., D.F., C.W. and A.C.; formal analysis, E.-A.M., V.S., C.W., C.P., R.I., C.I.R., L.B.-T. and A.S.; investigation, E.-A.M., V.S., C.W., C.P., R.I., C.I.R., L.B.-T. and A.S.; resources, D.S., D.F., C.S., A.C. and C.A.D.; data curation, E.-A.M., V.S., C.W., C.P., R.I., C.I.R. and L.B.-T.; writing—original draft preparation, E.-A.M. and V.S.; writing—review and editing, D.S., D.F., C.S., A.C. and C.A.D.; visualization, D.S., D.F., C.S., A.C. and C.A.D.; supervision, D.F., C.S., A.C. and C.A.D.; project administration, E.-A.M. and C.A.D. All authors have read and agreed to the published version of the manuscript.

Institutional Review Board Statement: Not applicable.

Informed Consent Statement: Not applicable.

Data Availability Statement: Authors can provide raw data upon request.

Conflicts of Interest: The authors declare no conflict of interest.

References

1. Global Cancer Observatory (GCO). Estimated Number of Deaths from 2020 to 2030, Both Sexes, Age [0–85+]. All Cancers. International Agency for Research on Cancer. World Health Organization. Available online: https://gco.iarc.fr (accessed on 19 September 2022).
2. Van der Meel, R.; Sulheim, E.; Shi, Y.; Kiessling, F.; Mulder, W.J.M.; Lammers, T. Smart cancer nanomedicine. *Nat. Nanotechnol.* **2019**, *14*, 1007–1017. [CrossRef] [PubMed]
3. Bhatia, S.N.; Chen, X.; Dobrovolskaia, M.A.; Lammers, T. Cancer nanomedicine. *Nat. Rev. Cancer* **2022**, *22*, 550–556. [CrossRef] [PubMed]
4. Tsiapla, A.-R.; Uzunova, V.; Oreshkova, T.; Angelakeris, M.; Samaras, T.; Kalogirou, O.; Tzoneva, R. Cell Behavioral Changes after the Application of Magneto-Mechanical Activation to Normal and Cancer Cells. *Magnetochemistry* **2022**, *8*, 21. [CrossRef]
5. Hosu, O.; Tertis, M.; Cristea, C. Implication of Magnetic Nanoparticles in Cancer Detection, Screening and Treatment. *Magnetochemistry* **2019**, *5*, 55. [CrossRef]
6. Bakshi, S.; Zakharchenko, A.; Minko, S.; Kolpashchikov, D.M.; Katz, E. Towards Nanomaterials for Cancer Theranostics: A System of DNA-Modified Magnetic Nanoparticles for Detection and Suppression of RNA Marker in Cancer Cells. *Magnetochemistry* **2019**, *5*, 24. [CrossRef]
7. De Oliveira, S.A.; Borges, R.; dos Santos Rosa, D.; de Souza, A.C.S.; Seabra, A.B.; Baino, F.; Marchi, J. Strategies for Cancer Treatment Based on Photonic Nanomedicine. *Materials* **2021**, *14*, 1435. [CrossRef]

8.　　Schirrmacher, V. From chemotherapy to biological therapy: A review of novel concepts to reduce the side effects of systemic cancer treatment (Review). *Int. J. Oncol.* **2019**, *54*, 407–419.

9.　　Lungu, I.I.; Grumezescu, A.M.; Volceanov, A.; Andronescu, E. Nanobiomaterials Used in Cancer Therapy: An Up-To-Date Overview. *Molecules* **2019**, *24*, 3547. [CrossRef]

10.　Yagawa, Y.; Tanigawa, K.; Kobayashi, Y.; Yamamoto, M. Cancer immunity and therapy using hyperthermia with immunotherapy, radiotherapy, chemotherapy, and surgery. *J. Cancer Metastasis Treat.* **2017**, *3*, 218–230. [CrossRef]

11.　Seegenschmiedt, M.H.; Vernon, C.C. A Historical Perspective on Hyperthermia in Oncology. In *Thermoradiotherapy and Thermochemotherapy: Biology, Physiology, Physics*; Seegenschmiedt, M.H., Fessenden, P., Vernon, C.C., Eds.; Medical Radiology; Springer: Berlin/Heidelberg, Germany, 1995; pp. 3–44. ISBN 978-3-642-57858-8.

12.　Yang, S.J.; Huang, C.H.; Wang, C.H.; Shieh, M.J.; Chen, K.C. The Synergistic Effect of Hyperthermia and Chemotherapy in Magnetite Nanomedicine-Based Lung Cancer Treatment. *Int. J. Nanomed.* **2020**, *15*, 10331–10347. [CrossRef]

13.　Jabalera, Y.; Sola-Leyva, A.; Carrasco-Jiménez, M.P.; Iglesias, G.R.; Jimenez-Lopez, C. Synergistic Photothermal-Chemotherapy Based on the Use of Biomimetic Magnetic Nanoparticles. *Pharmaceutics* **2021**, *13*, 625. [CrossRef] [PubMed]

14.　Van Vulpen, M.; De Leeuw, A.A.C.; Raaymakers, B.W.; Van Moorselaar, R.J.A.; Hofman, P.; Lagendijk, J.J.W.; Battermann, J.J. Radiotherapy and Hyperthermia in the Treatment of Patients with Locally Advanced Prostate Cancer: Preliminary Results. *BJU Int.* **2004**, *93*, 36–41. [CrossRef] [PubMed]

15.　Peeken, J.C.; Vaupel, P.; Combs, S.E. Integrating Hyperthermia into Modern Radiation Oncology: What Evidence Is Necessary? *Front. Oncol.* **2017**, *7*, 132–149. [CrossRef] [PubMed]

16.　Anscher, M.S.; Lee, C.; Hurwitz, H.; Tyler, D.; Prosnitz, L.R.; Jowell, P.; Rosner, G.; Samulski, T.; Dewhirst, M.W. A Pilot Study of Preoperative Continuous Infusion 5-Fluorouracil, External Microwave Hyperthermia, and External Beam Radiotherapy for Treatment of Locally Advanced, Unresectable, or Recurrent Rectal Cancer. *Int. J. Radiat. Oncol. Biol. Phys.* **2000**, *47*, 719–724. [CrossRef]

17.　Feyerabend, T.; Wiedemann, G.J.; Jäger, B.; Vesely, H.; Mahlmann, B.; Richter, E. Local Hyperthermia, Radiation, and Chemotherapy in Recurrent Breast Cancer Is Feasible and Effective except for Inflammatory Disease. *Int. J. Radiat. Oncol. Biol. Phys.* **2001**, *49*, 1317–1325. [CrossRef]

18.　Roti, J.L. Cellular responses to hyperthermia (40–46 °C): Cell killing and molecular events. *Int. J. Hyperth.* **2008**, *24*, 3–15. [CrossRef]

19.　Datta, N.R.; Ordóñez, S.G.; Gaipl, U.S.; Paulides, M.M.; Crezee, H.; Gellermann, J.; Marder, D.; Puric, E.; Bodis, S. Local Hyperthermia Combined with Radiotherapy And-/or Chemotherapy: Recent Advances and Promises for the Future. *Cancer Treat. Rev.* **2015**, *41*, 742–753. [CrossRef]

20.　Zhu, L.; Altman, M.B.; Laszlo, A.; Straube, W.; Zoberi, I.; Hallahan, D.E.; Chen, H. Ultrasound hyperthermia technology for radiosensitization. *Ultrasound. Med. Biol.* **2019**, *45*, 1025–1043. [CrossRef]

21.　Kobayashi, T. Cancer hyperthermia using magnetic nanoparticles. *Biotechnol. J.* **2011**, *6*, 1342–1347. [CrossRef]

22.　Storm, F.K.; Harrison, W.H.; Elliott, R.S.; Morton, D.L. Normal Tissue and Solid Tumor Effects of Hyperthermia in Animal Models and Clinical Trials. *Cancer Res.* **1979**, *39*, 2245–2251.

23.　Kok, H.P.; Cressman, E.N.K.; Ceelen, W.; Brace, C.L.; Ivkov, R.; Grüll, H.; ter Haar, G.; Wust, P.; Crezee, J. Heating Technology for Malignant Tumors: A Review. *Int. J. Hyperth.* **2020**, *37*, 711–741. [CrossRef] [PubMed]

24.　Perigo, E.A.; Hemery, G.; Sandre, O.; Ortega, D.; Garaio, E.; Plazaola, F.; Teran, F.J. Fundamentals and advances in magnetic hyperthermia. *Appl. Phys. Rev.* **2015**, *2*, 041302. [CrossRef]

25.　Fan, W.; Yung, B.; Huang, P.; Chen, X. Nanotechnology for multimodal synergistic cancer therapy. *Chem. Rev.* **2017**, *117*, 13566–13638. [CrossRef] [PubMed]

26.　Moacă, E.A.; Watz, C.G.; Socoliuc, V.; Racoviceanu, R.; Păcurariu, C.; Ianoş, R.; Cînta-Pînzaru, S.; Barbu Tudoran, L.; Nekvapil, F.; Iurciuc, S.; et al. Biocompatible Magnetic Colloidal Suspension Used as a Tool for Localized Hyperthermia in Human Breast Adenocarcinoma Cells: Physicochemical Analysis and Complex In Vitro Biological Profile. *Nanomaterials* **2021**, *11*, 1189. [CrossRef]

27.　Shabatina, T.I.; Vernaya, O.I.; Shabatin, V.P.; Melnikov, M.Y. Magnetic Nanoparticles for Biomedical Purposes: Modern Trends and Prospects. *Magnetochemistry* **2020**, *6*, 30. [CrossRef]

28.　Sun, C.; Lee, J.S.H.; Zhang, M. Magnetic nanoparticles in MR imaging and drug delivery. *Adv. Drug Deliv. Rev.* **2008**, *60*, 1252–1265. [CrossRef]

29.　Gobbo, O.L.; Sjaastad, K.; Radomski, M.W.; Volkov, Y.; Prina-Mello, A. Magnetic nanoparticles in cancer theranostics. *Theranostics* **2015**, *5*, 1249–1263. [CrossRef]

30.　Conde-Leboran, I.; Baldomir, D.; Martinez-Boubeta, C.; Chubykalo-Fesenko, O.; del Puerto Morales, M.; Salas, G.; Cabrera, D.; Camarero, J.; Teran, F.J.; Serantes, D. A Single Picture Explains Diversity of Hyperthermia Response of Magnetic Nanoparticles. *J. Phys. Chem. C* **2015**, *119*, 15698–15706. [CrossRef]

31.　Shen, L.; Li, B.; Qiao, Y. Fe_3O_4 nanoparticles in targeted drug/gene delivery systems. *Materials* **2018**, *11*, 324. [CrossRef]

32.　Xie, L.; Jin, W.; Zuo, X.; Ji, S.; Nan, W.; Chen, H.; Gao, S.; Zhang, Q. Construction of small-sized superparamagnetic Janus nanoparticles and their application in cancer combined chemotherapy and magnetic hyperthermia. *Biomater. Sci.* **2020**, *8*, 1431–1441. [CrossRef] [PubMed]

33. Rajan, A.; Sahu, N.K. Review on magnetic nanoparticle-mediated hyperthermia for cancer therapy. *J. Nanopart. Res.* **2020**, *22*, 1–25. [CrossRef]

34. Martinez-Boubeta, C.; Simeonidis, K.; Oró, J.; Makridis, A.; Serantes, D.; Balcells, L. Finding the Limits of Magnetic Hyperthermia on Core-Shell Nanoparticles Fabricated by Physical Vapor Methods. *Magnetochemistry* **2021**, *7*, 49. [CrossRef]

35. Gupta, R.; Kaur, T.; Chauhan, A.; Kumar, R.; Kuanr, B.K.; Sharma, D. Tailoring nanoparticles design for enhanced heating efficiency and improved magneto-chemo therapy for glioblastoma. *Biomater. Adv.* **2022**, *139*, 213021. [CrossRef] [PubMed]

36. Soltys, L.; Olkhovyy, O.; Tatarchuk, T.; Naushad, M. Green Synthesis of Metal and Metal Oxide Nanoparticles: Principles of Green Chemistry and Raw Materials. *Magnetochemistry* **2021**, *7*, 145. [CrossRef]

37. Vijayaraghavan, K.; Ashokkumar, T. Plant-mediated Biosynthesis of Metallic Nanoparticles: A Review of Literature, Factors Affecting Synthesis, Characterization Techniques and Applications. *J. Environ. Chem. Eng.* **2017**, *5*, 4866–4883. [CrossRef]

38. Mirza, A.U.; Kareem, A.; Nami, S.A.; Khan, M.S.; Rehman, S.; Bhat, S.A.; Mohammad, A.; Nishat, N. Biogenic Synthesis of Iron Oxide Nanoparticles Using Agrewia Optiva and Prunus Persica Phyto Species: Characterization, Antibacterial and Antioxidant Activity. *J. Photochem. Photobiol. B Biol.* **2018**, *185*, 262–274. [CrossRef]

39. Latif, M.S.; Abbas, S.; Kormin, F.; Mustafa, M.K. Green Synthesis of Plant-Mediated Metal Nanoparticles: The Role of Polyphenols. *Asian J. Pharmaceut. Clin. Res.* **2019**, *12*, 75–84. [CrossRef]

40. Gahlawat, G.; Choudhury, A.R. A Review on the Biosynthesis of Metal and Metal Salt Nanoparticles by Microbes. *RSC Adv.* **2019**, *9*, 12944–12967. [CrossRef]

41. Vasantharaj, S.; Sathiyavimal, S.; Senthilkumar, P.; Lewis Oscar, F.; Pugazhendhi, A. Biosynthesis of Iron Oxide Nanoparticles Using Leaf Extract of Ruellia Tuberosa: Antimicrobial Properties and Their Applications in Photocatalytic Degradation. *J. Photochem. Photobiol. B Biol.* **2019**, *192*, 74–82. [CrossRef]

42. Singh, J.; Dutta, T.; Kim, K.H.; Rawat, M.; Samddar, P.; Kumar, P. 'Green'synthesis of Metals and Their Oxide Nanoparticles: Applications for Environmental Remediation. *J. Nanobiotechnol.* **2018**, *16*, 84. [CrossRef]

43. Mondal, P.; Anweshan, A.; Purkait, M.K. Green Synthesis and Environmental Application of Iron-Based Nanomaterials and Nanocomposite: A Review. *Chemosphere* **2020**, *259*, 127509. [CrossRef] [PubMed]

44. Khalil, A.T.; Ovais, M.; Ullah, I.; Ali, M.; Shinwari, Z.K.; Maaza, M. Biosynthesis of Iron Oxide (Fe2O3) Nanoparticles via Aqueous Extracts of Sageretia Thea (Osbeck.) and Their Pharmacognostic Properties. *Green. Chem. Lett. Rev.* **2017**, *10*, 186–201. [CrossRef]

45. Arularasu, M.V.; Devakumar, J.; Rajendran, T.V. An Innovative Approach for green Synthesis of Iron Oxide Nanoparticles: Characterization and its Photocatalytic Activity. *Polyhedron* **2018**, *156*, 279–290. [CrossRef]

46. Bibi, I.; Nazar, N.; Ata, S.; Sultan, M.; Ali, A.; Abbas, A.; Jilani, K.; Kamal, S.; Sarim, F.M.; Khan, M.I.; et al. Green Synthesis of Iron Oxide Nanoparticles Using Pomegranate Seeds Extract and Photocatalytic Activity Evaluation for the Degradation of Textile Dye. *J. Mater. Res. Technol.* **2019**, *8*, 6115–6124. [CrossRef]

47. Abdullah, J.A.A.; Eddine, L.S.; Abderrhmane, B.; Alonso-González, M.; Guerrero, A.; Romero, A. Green Synthesis and Characterization of Iron Oxide Nanoparticles by Pheonix Dactylifera Leaf Extract and Evaluation of Their Antioxidant Activity. *Sust. Chem. Pharm.* **2020**, *17*, 100280. [CrossRef]

48. Yew, Y.P.; Shameli, K.; Miyake, M.; Ahmad Khairudin, N.B.B.; Mohamad, S.E.B.; Naiki, T.; Lee, K.X. Green biosynthesis of superparamagnetic magnetite Fe3O4 nanoparticles and biomedical applications in targeted anticancer drug delivery system: A review. *Arab. J. Chem.* **2020**, *13*, 2287–2308. [CrossRef]

49. Nadeem, A.; Ali, J.S.; Latif, M.; Rizvi, Z.F.; Naz, S.; Mannan, A.; Zia, M. Green synthesis and characterization of Fe, Cu and Mg oxide nanoparticles using Clematis orientalis leaf extract: Salt concentration modulates physiological and biological properties. *Mater. Chem. Phys.* **2021**, *271*, 124900. [CrossRef]

50. El Badawy, A.M.; Luxton, T.P.; Silva, R.G.; Scheckel, K.G.; Suidan, M.T.; Tolaymat, T.M. Impact of environmental conditions (pH, ionic strength, and electrolyte type) on the surface charge and aggregation of silver nanoparticles suspensions. *Environ. Sci. Technol.* **2010**, *44*, 1260–1266. [CrossRef]

51. Shah, M.; Fawcett, D.; Sharma, S.; Tripathy, S.K.; Poinern, G.E.J. Green synthesis of metallic nanoparticles via biological entities. *Materials* **2015**, *8*, 7278–7308. [CrossRef]

52. Singh, P.; Kim, Y.J.; Zhang, D.; Yang, D.C. Biological synthesis of nanoparticles from plants and microorganisms. *Trends Biotechnol.* **2016**, *34*, 588–599. [CrossRef]

53. Bora, K. Phytochemical and pharmacological potential of Artemisia absinthium Linn. *and Artemisia asiatica Nakai: A Review. J. Pharm. Res.* **2010**, *3*, 325–328.

54. Taleghani, A.; Emami, S.A.; Tayarani-Najaran, Z. Artemisia: A promising plant for the treatment of cancer. *Bioorg. Med. Chem.* **2020**, *28*, 115180. [CrossRef] [PubMed]

55. Szopa, A.; Pajor, J.; Klin, P.; Rzepiela, A.; Elansary, H.O.; Al-Mana, F.A.; Mattar, M.A.; Ekiert, H. *Artemisia absinthium* L. —Importance in the History of Medicine, the Latest Advances in Phytochemistry and Therapeutical, Cosmetological and Culinary Uses. *Plants* **2020**, *9*, 1063. [CrossRef] [PubMed]

56. Moacă, A.E.; Pavel, I.Z.; Danciu, C.; Crăiniceanu, Z.; Minda, D.; Ardelean, F.; Antal, D.S.; Ghiulai, R.; Cioca, A.; Derban, M.; et al. Romanian Wormwood (*Artemisia absinthium* L.): Physicochemical and Nutraceutical Screening. *Molecules* **2019**, *24*, 3087. [CrossRef] [PubMed]

57. Asghar, M.N.; Khan, I.U.; Bano, N. In vitro antioxidant and radical-scavenging capacities of Citrullus colocynthes (L) and Artemisia absinthium extracts using promethazine hydrochloride radical cation and contemporary assays. *Food Sci. Technol. Int.* **2011**, *17*, 481–494. [CrossRef]

58. Guarrera, P.M. Traditional antihelmintic, antiparasitic and repellent uses of plants in Central Italy. *J. Ethnopharmacol.* **1999**, *68*, 183–192. [CrossRef]

59. Kharoubi, O.; Slimani, M.; Aoues, A. Neuroprotective effect of wormwood against lead exposure. *J. Emerg. Trauma Shock* **2011**, *4*, 82. [CrossRef]

60. Minda, D.; Ghiulai, R.; Banciu, C.D.; Pavel, I.Z.; Danciu, C.; Racoviceanu, R.; Soica, C.; Budu, O.D.; Muntean, D.; Diaconeasa, Z.; et al. Phytochemical Profile, Antioxidant and Wound Healing Potential of Three Artemisia Species: In Vitro and In Ovo Evaluation. *Appl. Sci.* **2022**, *12*, 1359. [CrossRef]

61. Silva, M.P.; Drummond, A.L.; Aquino, V.R.R.; Silva, L.P.; Azevedo, R.B.; Sales, M.J.A.; Morais, P.C.; Bakuzisc, A.F.; Sousa, M.H. Facile green synthesis of nanomagnets for modulating magnetohyperthermia: Tailoring size, shape and phase. *RSC Adv.* **2017**, *7*, 47669–47671. [CrossRef]

62. Ramirez-Nuñez, A.L.; Jimenez-Garcia, L.F.; Goya, G.F.; Sanz, B.; Santoyo-Salazar, J. In vitro magnetic hyperthermia using polyphenol-coated $Fe_3O_4@\gamma Fe_2O_3$ nanoparticles from Cinnamomun verum and Vanilla planifolia: The concert of green synthesis and therapeutic possibilities. *Nanotechnology* **2018**, *29*, 074001–074034. [CrossRef]

63. Koli, R.R.; Phadatare, M.R.; Sinha, B.B.; Sakate, D.M.; Ghule, A.V.; Ghodake, G.S.; Deshpande, N.G.; Fulari, V.J. Gram bean extract-mediated synthesis of Fe_3O_4 nanoparticles for tuning the magneto-structural properties that influence the hyperthermia performance. *J. Taiwan Inst. Chem. Eng.* **2019**, *95*, 357–368. [CrossRef]

64. Karade, V.C.; Parit, S.B.; Dawkar, V.V.; Devan, R.S.; Choudhary, R.J.; Kedge, V.V.; Pawar, N.V.; Kim, J.H.; Chougale, A.D. A green approach for the synthesis of α-Fe_2O_3 nanoparticles from Gardenia resinifera plant and it's in vitro hyperthermia application. *Heliyon* **2019**, *5*, e02044. [CrossRef] [PubMed]

65. Yusefi, M.; Shameli, K.; Su Yee, O.; Teow, S.Y.; Hedayatnasab, Z.; Jahangirian, H.; Webster, T.J.; Kuča, K. Green Synthesis of Fe_3O_4 Nanoparticles Stabilized by a Garcinia mangostana Fruit Peel Extract for Hyperthermia and Anticancer Activities. *Int. J. Nanomed.* **2021**, *16*, 2515–2532. [CrossRef]

66. Yusefi, M.; Shameli, K.; Hedayatnasab, Z.; Teow, S.Y.; Ismail, U.N.; Azlan, C.A.; Ali, R.R. Green synthesis of Fe_3O_4 nanoparticles for hyperthermia, magnetic resonance imaging and 5-fluorouracil carrier in potential colorectal cancer treatment. *Res. Chem. Intermed.* **2021**, *47*, 1789–1808. [CrossRef]

67. Rezanezhad, A.; Hajalilou, A.; Eslami, F.; Parvini, E.; Abouzari-Lotf, E.; Aslibeiki, B. Superparamagnetic magnetite nanoparticles for cancer cells treatment via magnetic hyperthermia: Effect of natural capping agent, particle size and concentration. *J. Mater. Sci. Mater. Electron.* **2021**, *32*, 24026–24040. [CrossRef]

68. El-Rafie, H.M.; Abd El-Aziz, S.M.; Zahran, M.K. In vitro cytotoxicity against breast cancer using biogenically synthesized gold and iron oxide nanoparticles derived from the hydroethanolic extract of *Salvia officinalis* L. *Chem. Pap.* **2022**, *2022.*, 1–13. [CrossRef]

69. Mai, T.; Hilt, J.Z. Functionalization of iron oxide nanoparticles with small molecules and the impact on reactive oxygen species generation for potential cancer therapy. *Colloids Surf. A Physicochem. Eng. Asp.* **2019**, *576*, 9–14. [CrossRef]

70. Basavegowda, N.; Somai Magar, K.B.; Mishra, K.; Lee, Y.R. Green fabrication of ferromagnetic Fe_3O_4 nanoparticles and their novel catalytic applications for the synthesis of biologically interesting benzoxazinone and benzthioxazinone derivatives. *New J. Chem.* **2014**, *38*, 5415–5420. [CrossRef]

71. Yew, Y.P.; Shameli, K.; Miyake, M.; Kuwano, N.; Ahmad Khairudin, N.B.; Mohamad, S.E.; Lee, K.X. Green synthesis of magnetite (Fe_3O_4) nanoparticles using seaweed (*Kappaphycus alvarezii*) extract. *Nano Res. Lett.* **2016**, *11*, 276. [CrossRef]

72. Rajiv, P.; Bavadharani, B.; Naveen Kumar, M.; Vanathi, P. Synthesis and characterization of biogenic iron oxide nanoparticles using green chemistry approach and evaluating their biological activities. *Biocatal. Agric. Biotechnol.* **2017**, *12*, 45–49. [CrossRef]

73. Abdullah, M.M.S.; Atta, A.M.; Allohedan, H.A.; Alkhathlan, H.Z.; Khan, M.; Ezzat, A.O. Green Synthesis of Hydrophobic Magnetite Nanoparticles Coated with Plant Extract and Their Application as Petroleum Oil Spill Collectors. *Nanomaterials* **2018**, *8*, 855. [CrossRef] [PubMed]

74. Ferreira, L.P.; Reis, C.P.; Robalo, T.T.; Melo Jorge, M.E.; Ferreira, P.; Gonçalves, J.; Hajalilou, A.; Cruz, M.M. Assisted Synthesis of Coated Iron Oxide Nanoparticles for Magnetic Hyperthermia. *Nanomaterials* **2022**, *12*, 1870. [CrossRef] [PubMed]

75. Karthik, S.; Suriyaprabha, R.; Vinoth, M.; Srither, S.R.; Manivasakan, P.; Rajendran, V.; Valiyaveettil, S. Larvicidal, super hydrophobic and antibacterial properties of herbal nanoparticles from Acalypha indica for biomedical applications. *RSC Adv.* **2017**, *7*, 41763–41770.

76. Kim, W.; Suh, C.Y.; Cho, S.W.; Roh, K.M.; Kwon, H.; Song, K.; Shon, I.J. A new method for the identification and quantification of magnetite–maghemite mixture using conventional X-ray diffraction technique. *Talanta* **2012**, *94*, 348–352. [CrossRef] [PubMed]

77. Roy, K.; Sarkar, C.K.; Ghosh, C.K. Green synthesis of silver nanoparticles using fruit extract of malus domestica and study of its antimicrobial activity. *Dig. J. Nanomater. Biostructures* **2014**, *9*, 1137–1147.

78. Hemalatha, K.; Alamelumangai, K.; Arulmozhi, R.; Chandunika, R.K.; Sahu, N.K.; Parthipan, G.; Rajaram, M. Cytotoxic effect of functionalized superparamagnetic samarium doped iron oxide nanoparticles for hyperthermia application. *Ceram. Int.* **2022**, *48*, 24485–24495. [CrossRef]

79. Lunge, S.; Singh, S.; Sinha, A. Magnetic iron oxide (Fe_3O_4) nanoparticles from tea waste for arsenic removal. *J. Magn. Magn. Mater.* **2014**, *356*, 21–31. [CrossRef]

80. Prasad, C.; Gangadhara, S.; Venkateswarlu, P. Bio-inspired green synthesis of Fe₃O₄ magnetic nanoparticles using watermelon rinds and their catalytic activity. *Appl. Nanosci.* **2016**, *6*, 797–802. [CrossRef]
81. Izadiyan, Z.; Shameli, K.; Miyake, M.; Hara, H.; Binti Mohamad, S.E.; Kalantari, K.; Mohd Taib, S.H.; Rasouli, E. Cytotoxicity assay of plant-mediated synthesized iron oxide nanoparticles using Juglans regia green husk extract. *Arab. J. Chem.* **2020**, *13*, 2011–2023. [CrossRef]
82. Li, X.; Xu, H.; Chen, Z.S.; Chen, G. Biosynthesis of nanoparticles by microorganisms and their applications. *J. Nanomater.* **2011**, *2011*, 270974. [CrossRef]
83. Smuleac, V.; Varma, R.; Sikdar, S.; Bhattacharyyaa, D. Green synthesis of Fe and Fe/Pd bimetallic nanoparticles in membranes for reductive degradation of chlorinated organics. *J. Membr. Sci.* **2011**, *379*, 131–137. [CrossRef]
84. Makarov, V.V.; Love, A.J.; Sinitsyna, O.V.; Makarova, S.S.; Yaminsky, I.V.; Taliansky, M.E.; Kalinina, N.O. Green Nanotechnologies: Synthesis of Metal Nanoparticles Using Plants. *Acta Nat.* **2014**, *6*, 35–45. [CrossRef]
85. Cruz, D.; Fale, P.L.; Mourato, A.; Vaz, P.D.; Serralheiro, M.L.; Lino, A.R.L. Preparation and physicochemical characterization of Ag nanoparticles biosynthesized by Lippia citriodora (*Lemon verbena*). *Colloids Surf. B Biointerfaces* **2010**, *81*, 67–73. [CrossRef] [PubMed]
86. Rao, N.H.; Lakshmidevi, N.; Pammi, S.V.N.; Kollu, P.; Ganapaty, S.; Lakshmi, P. Green synthesis of silver nanoparticles using methanolic root extracts of Diospyros paniculata and their antimicrobial activities. *Mat. Sci. Eng. C* **2016**, *62*, 553–557. [CrossRef] [PubMed]
87. Rosensweig, R.E. *Ferrohydrodynamics*; Cambridge Univ. Press: Cambridge, UK, 1985; p. 344.
88. Tombácz, E.; Turcu, R.; Socoliuc, V.; Vekas, L. Magnetic iron oxide nanoparticles: Recent trends in design and synthesis of magnetoresponsive nanosystems. *Biochem. Biophys. Res. Commun.* **2015**, *468*, 442–453. [CrossRef]
89. Moacă, E.A.; Watz, C.G.; Flondor Ionescu, D.; Păcurariu, C.; Tudoran, L.B.; Ianoș, R.; Socoliuc, V.; Drăghici, G.A.; Iftode, A.; Liga, S.; et al. Biosynthesis of Iron Oxide Nanoparticles: Physico-Chemical Characterization and Their In Vitro Cytotoxicity on Healthy and Tumorigenic Cell Lines. *Nanomaterials* **2022**, *12*, 2012. [CrossRef] [PubMed]
90. Socoliuc, V.; Vekas, L.; Turcu, R. Magnetically in-duced phase condensation in an aqueous dispersion of magnetic nanogels. *Soft Matter* **2013**, *9*, 3098–3105. [CrossRef]
91. Wildeboer, R.R.; Southern, P.; Pankhurst, Q.A. On the reliable measurement of specific absorption rates and intrinsic loss parameters in magnetic hyperthermia materials. *J. Phys. D Appl. Phys.* **2014**, *47*, 495003–495017. [CrossRef]
92. Available online: https://en.wikipedia.org/wiki/List_of_thermal_conductivities (accessed on 22 September 2022).